True dipole wander

Peter Olson, Maylis Landeau, Evan Reynolds

Geophysical Journal International

Geophys. J. Int. (2018) **215,** 1523–1529
Advance Access publication 2018 August 25
GJI Geomagnetism, rock magnetism and palaeomagnetism

doi: 10.1093/gji/ggy349

EXPRESS LETTER

True dipole wander

Peter Olson,[1,2] Maylis Landeau[3] and Evan Reynolds[4]

[1]*Department of Earth and Planetary Sciences, Johns Hopkins University, Baltimore, MD 21218, USA. E-mail: olson@jhu.edu*
[2]*Department of Earth & Planetary Sciences, University of New Mexico, Albuquerque, NM 87131, USA*
[3]*Department of Applied Mathematics and Theoretical Physics, Cambridge University, Cambridge CB3 0WA, UK*
[4]*T-Mobile USA, Bellevue WA 98006, USA*

Accepted 2018 August 23. Received 2018 August 17; in original form 2018 March 20

SUMMARY

A fundamental assumption in palaeomagnetism is that the geomagnetic field closely approximates a geocentric axial dipole in time average. Here we use numerical dynamos driven by heterogeneous core–mantle boundary heat flux from a mantle global circulation model to demonstrate how mantle convection produces true dipole wander, rotation of the geomagnetic dipole on geologic timescales. Our heterogeneous mantle-driven dynamos show a dipole rotation about a near-equatorial axis in response to the transition in lower mantle heterogeneity from a highly asymmetric pattern at the time of supercontinent Pangea to a more symmetric pattern today. This predicted dipole rotation overlaps with a palaeomagnetically inferred rotation in the opposite direction and suggests that some events previously interpreted as true polar wander also include true dipole wander.

Key words: Core; Mantle processes; Dynamo theories and simulations; Palaeomagnetism; Reversals; Dynamics: convection currents and mantle plumes.

1 INTRODUCTION

When using palaeomagnetic data for reconstructing plate tectonics, continent locations and palaeoclimates, it is generally assumed that the geomagnetic field consists of a geocentric axial dipole when averaged over sufficiently long times. Tested against palaeomagnetic directions from the recent past, this assumption is found to be accurate within a few degrees (Schneider & Kent 1990; McElhinny *et al.* 1996) and it is also qualitatively supported by older palaeomagnetic data when averaged over many hundreds of million years (Evans 2003; Veikkolainen & Pesonen 2014). Nevertheless, there is palaeomagnetic evidence favouring small yet long-lasting axial quadrupole and octupole geomagnetic field components with amplitudes equal to a few per cent of the dipole (Johnson *et al.* 2008), broadly consistent with the time average fields produced by numerical dynamos, which often show persistent axial octupole components coexisting with the axial dipole that depend on inner core size, boundary heterogeneity and other effects (Bloxham 2000; Heimpel & Evans 2013; Landeau *et al.* 2017).

Non-axisymmetric geomagnetic field components are more troublesome for tectonic and palaeoclimate reconstructions that assume an axial geocentric dipole because they produce longitudinally dependent errors in palaeolatitude. Yet, there is abundant evidence for long-lasting non-axisymmetric geomagnetic field components. Time averages of the geomagnetic field show measurable deviations from axisymmetry on century (Gillet *et al.* 2013) and millennium timescales (Korte & Holme 2010), and there are also dipole tilt variations on millennial timescales (Nilsson *et al.* 2011). Palaeomagnetic evidence for similar deviations on million year timescales (Johnson & Constable 1997; Kelly & Gubbins 1997) remains controversial (Johnson & McFadden 2015). Significantly, the same numerical dynamos that produce symmetric time average magnetic fields with symmetric boundary heterogeneity yield asymmetric time average magnetic fields with inclined dipoles when asymmetric boundary conditions are applied (Olson & Deguen 2012; Olson *et al.* 2017).

In this paper, we analyse numerical dynamos driven by heterogeneous outer boundary heat flux that produce long-lasting deviations of the magnetic dipole axis relative to the planetary spin axis. By long-lasting we mean deviations that persist when the magnetic field and its dipole axis orientation are averaged over multiple dipole free decay times, equivalent to several hundred thousand years in Earth's core. This is far longer than the characteristic timescales for variability of the circulation in Earth's core (measured in hundreds or thousands of years), far shorter than the characteristic timescales for variability of the circulation in Earth's mantle (measured in tens or hundreds of millions of years) but comparable to the timescales represented by palaeomagnetic measurements. By averaging over this amount of time separately in both magnetic polarities, reverse and normal, while excluding polarity transitions when the field is non-dipolar, we suppress transient dipole fluctuations that are intrinsic to the dynamo process while highlighting the influence of boundary

heterogeneity on timescales commensurate with the interpretations of palaeomagnetic data.

Because convection in Earth's mantle is time-dependent, the geomagnetic dipole axis is expected to slowly rotate as the heat flux at the core–mantle boundary (CMB) varies. We use the term true dipole wander for the motions of the geomagnetic pole on these timescales. Fig. 1 is a schematic depiction of true dipole wander and the related phenomenon, true polar wander. With true dipole wander (panel a) the geomagnetic dipole rotates relative to the lithosphere and mantle, Earth's spin axis and the climate equator. With true polar wander (panel b) the lithosphere and continents (and likely the bulk of the mantle) rotate relative to the geomagnetic dipole, Earth's spin axis and the climate equator.

2 DIPOLE TILT FROM HETEROGENEOUS BOUNDARY HEAT FLUX

Fig. 2 illustrates long-lasting dipole tilt obtained using numerical dynamo code MagIC (Wicht 2002) with control parameters $Ek = 1 \times 10^{-4}$, $Ra = 4 \times 10^7$, $Pr = 1$ and $Pm = 6$ for the Ekman, Rayleigh, Prandtl and magnetic Prandtl numbers (Olson *et al.* 2017), in which the heat flux on the outer boundary (radius $r = 1$) has the spherical harmonic Y21 (degree $\ell = 2$ and order $m = 1$) pattern of variation shown in Fig. 2(a), with its peak-to-peak amplitude q^*_{Y21} normalized by the spherical average buoyancy flux on the inner dynamo boundary (radius $r = 0.35$). For these dynamos, the spherical average heat flux on the outer boundary is zero, modelling adiabatic thermal stratification below the CMB, and the dimensionless heat sink $\varepsilon = -0.8$ models thermochemical convection dominated by light element release from the inner core. For the dynamos in Fig. 2, the heat flux amplitude is varied between arbitrarily wide limits in order to quantify how the dipole axis tilt angle increases with q^*_{Y21}; in the next section we constrain the boundary heat flux heterogeneity using a mantle global circulation model (GCM).

The elevated heat flux regions on the outer boundary produce convective downwellings shown as blue patches in Fig. 2(b). These downwellings concentrate the magnetic field into intense off-axis spots located at high latitudes in both northern and southern hemispheres, and yielding the dipole axis location shown by the red cross in Fig. 2(c). Figs 2(d) and (e) show that the tilt angle of the dipole axis of the time average field increases quasi-linearly with the amplitude of the boundary heat flux heterogeneity q^*_{Y21}, whereas the dipole axis longitude is less sensitive to the amount of boundary heterogeneity. The error bars in Fig. 2(d) indicate standard deviations of the instantaneous dipole co-latitudes. Although the instantaneous dipole axis locations are highly variable in these dynamos, we show in the Supplementary Information that there is a little difference between the dipole axis location of the time average field and the time average location of the dipole axis when the non-dipole fields during polarity reversals are excluded.

3 TRUE DIPOLE WANDER FOLLOWING PANGEA BREAKUP

Fig. 3 shows the large-scale pattern of CMB heat flux at four epochs from a mantle GCM constrained by plate motions (Rudolph & Zhong 2014; Zhong & Rudolph 2015) along with the time average radial magnetic field intensity on the outer boundary of a numerical dynamo driven by each heat flux pattern. Except for the patterns of heat flux heterogeneity, we use the same dynamo parameters and the same evolutionary scheme as Olson *et al.* (2013) to model the geodynamo from the present day to 225 Ma. We combine the CMB heat flux predicted by the mantle GCM with thermal evolution of the core (Labrosse 2003), computing the evolution of the dynamo control parameters relative to their present-day values. We then tie this evolution to a present-day geodynamo model with parameters $Pr = 1$, $Pm = 20$ and $Ek = 5.75 \times 10^{-3}$, tuning Ra until the dynamo polarity reversal frequency matches the geomagnetic average over the past 5 million years. There are advantages in using reversing dynamos for simulating geomagnetic dipole wander. If a numerical dynamo fails to reverse polarity, it often means that its dipole field is too stable in the axial position, and consequently, its response to boundary heat flux heterogeneity is likely to be unrealistically weak. Another advantage of our dynamos is that they lie within the region of Earth-like behaviour as defined by Christensen *et al.* (2010) based on criteria such as dipolarity, secular variation and magnetic flux concentrations. For example, the dipolarity of these dynamos, the ratio of the rms dipole intensity to the rms total field intensity on the outer boundary, tends to decrease from present-day Earth-like values near 0.55 at times when the dipole axis tilt is small to near 0.4 when the dipole axis tilt is large.

At 0 and 75 Ma in Fig. 3, the time average dynamo magnetic fields are nearly symmetric and the dipole axes of their time average fields nearly coincide with the rotation axis. At 125 and 200 Ma, however, the time average fields are markedly less symmetric, with two asymmetrically located patches of high-intensity field, one northern and one southern, that tilt the dipole axis away from the rotation axis by about 15°. The key element in the boundary heterogeneity that produces this dipole tilt is the extensive region of elevated heat flux centred along 90°E Longitude in the northern hemisphere, produced by the downwelling in the mantle GCM located beneath a major subduction zone that formed on the northeastern margin of Pangea. This structure tends to weaken over time following Pangea breakup, and as it weakens the CMB heat flux becomes more uniform overall, the dynamo becomes more symmetric, and its time average magnetic field becomes more axial. For example, the peak CMB heat flux in this region diminishes from 169 mW m^{-2} at 200 Ma when dipole tilt is large to 89 mW m^{-2} at 0 Ma, while the rms CMB heat flux heterogeneity diminishes from 37 to 23 mW m^{-2} over the same time interval.

We have calculated dipole axis locations for the time average dynamo magnetic field from 225 to 0 Ma (present day) at epochs spaced 25 Ma apart, using the CMB heat flux patterns from the mantle GCM. The results are shown in Fig. 4(a) for normal magnetic polarity and in Fig. 4(b) for reverse magnetic polarity at the same epochs, except during the Cretaceous Normal Superchron (epochs 115 and 100 Ma). Closely consistent results are found in both polarities, the small differences between normal polarity and reverse polarity dipole locations being attributable to the finite averaging time used, approximately four dipole free decay times at each epoch. In addition, the dipole locations of the time average fields shown in Fig. 4 closely match the time averages of the instantaneous dipole locations (see the Supplementary Information).

At 200 Ma in Fig. 4(a) the geomagnetic pole (dipole axis location) lies approximately 14° from the spin axis. First it rotates 7° back towards the spin axis by 175 Ma, followed by a 10° rotation away from the spin axis by 125 Ma. Then, starting around 125 Ma, the geomagnetic pole migrates towards the spin axis along a generally east-to-west path (Fig. 4a). This motion amounts to approximately 17° of anticlockwise rotation of the dipole about an axis located near the equator and 0° Longitude. According to the normal polarity results in Fig. 4(a), the implied rates of true dipole wander lie in the

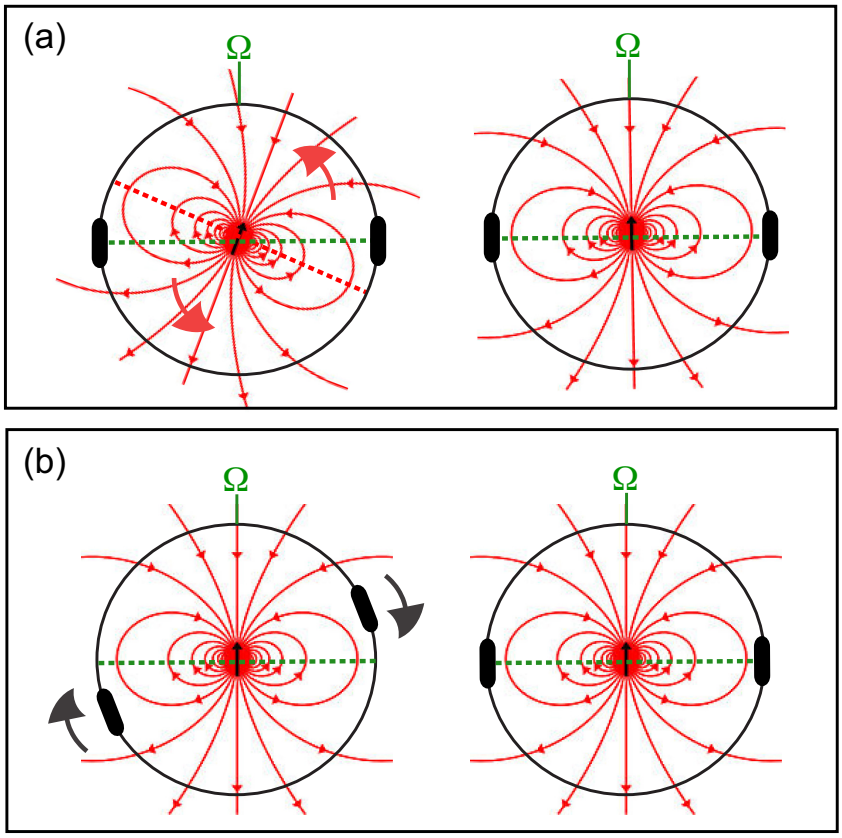

Figure 1. (a) True dipole wander. The geomagnetic dipole (red field lines with black central vector) rotates relative to the lithosphere (including continents) and the mantle (black perimeter), Earth's spin axis (Ω) and the climate equator (green). (b) True polar wander. The lithosphere (including continents) and the mantle rotate relative to the geomagnetic dipole, Earth's rotation axis and the climate equator.

range of 0.1°–0.8° of rotation per million years. A comparable set of dipole rotations are seen in Fig. 4(b) for reverse polarity times, the major differences being the 125 Ma dipole axis is tilted 20° from the spin axis, and there is no intermediate dipole axis location at 115 Ma. As a result, according to Fig. 4(b), the major anticlockwise dipole rotation is nearly 20° about an axis located very near the equator and 0° Longitude, with an implied (minimum) rotation rate of 0.4° per million years.

Interpreting Figs 4(a) and (b) more broadly, there are two clusters of geomagnetic pole locations, an off-axis cluster with older ages (red diamonds) and a near-axis cluster with younger ages (blue diamonds), the two clusters separated by 10°–20° of anticlockwise dipole rotation. According to this broader interpretation, the speed of the dipole rotation is uncertain, but the intermediate normal pole location at 115 Ma (green diamond) roughly gives the epoch when the dipole rotation was fastest.

The underlying causes of the dipolar motions implied by Figs 3 and 4(a) and (b) are temporal changes in the magnitude and pattern of the CMB heat flux that is asymmetric with respect to Earth's spin axis. To demonstrate this, Fig. 4(c) shows the time variation of the amplitude of the Y21 component of the CMB heat flux from the mantle GCM between 0 and 250 Ma compared to the dipole tilt calculated from our dynamos at each epoch, for both normal and reverse polarities. Here we are assuming that the Y21 component is a good proxy for the asymmetry of the CMB heat flux with respect to Earth's spin axis. Prior to 125 Ma, the Y21 CMB heat flux is generally large and its time variation roughly correlates with the variations in amplitude of the dipole tilt. After 125 Ma, in contrast, both the Y21 CMB heat flux and the dipole tilt are uniformly small.

4 DIPOLE WANDER VERSUS POLAR WANDER

True polar wander has been inferred at multiple times in the Phanerozoic on the basis of palaeomagnetic directions and other observations (Jurdy & Van der Voo 1975; Besse & Courtillot 2002; Evans 2003). Using palaeomagnetic directions, Steinberger & Torsvik (2008) identified a major Mesozoic polar wander event between 195 and 145 Ma on the basis of an apparent 18° clockwise rotation of the continents about a near-equatorial axis located between 10°W and 20°W Longitude. Torsvik *et al.* (2012) later identified multiple episodes of continent rotation between 250 and 100 Ma, including two successive Mesozoic rotations between 200 and 140 Ma amounting to nearly 30° of clockwise continent rotation about a near-equatorial axis located at approximately 11°E Longitude, implying rotation rates of 0.45°–0.8° per million years. Kent *et al.* (2015) constrained the timing of the major clockwise Mesozoic rotation to lie between 160 and 145 Ma with nearly 30° rotation, implying rotation rates near 1.5° per million years. Subsequently, Fu & Kent (2018) inferred an approximately 15° clockwise rotation of the Pacific Plate during 157–147 Ma using palaeolatitude determinations from core samples from old Pacific crust, generally consistent with their previously identified major Mesozoic clockwise rotation of the continents and demonstrating the global nature of this event.

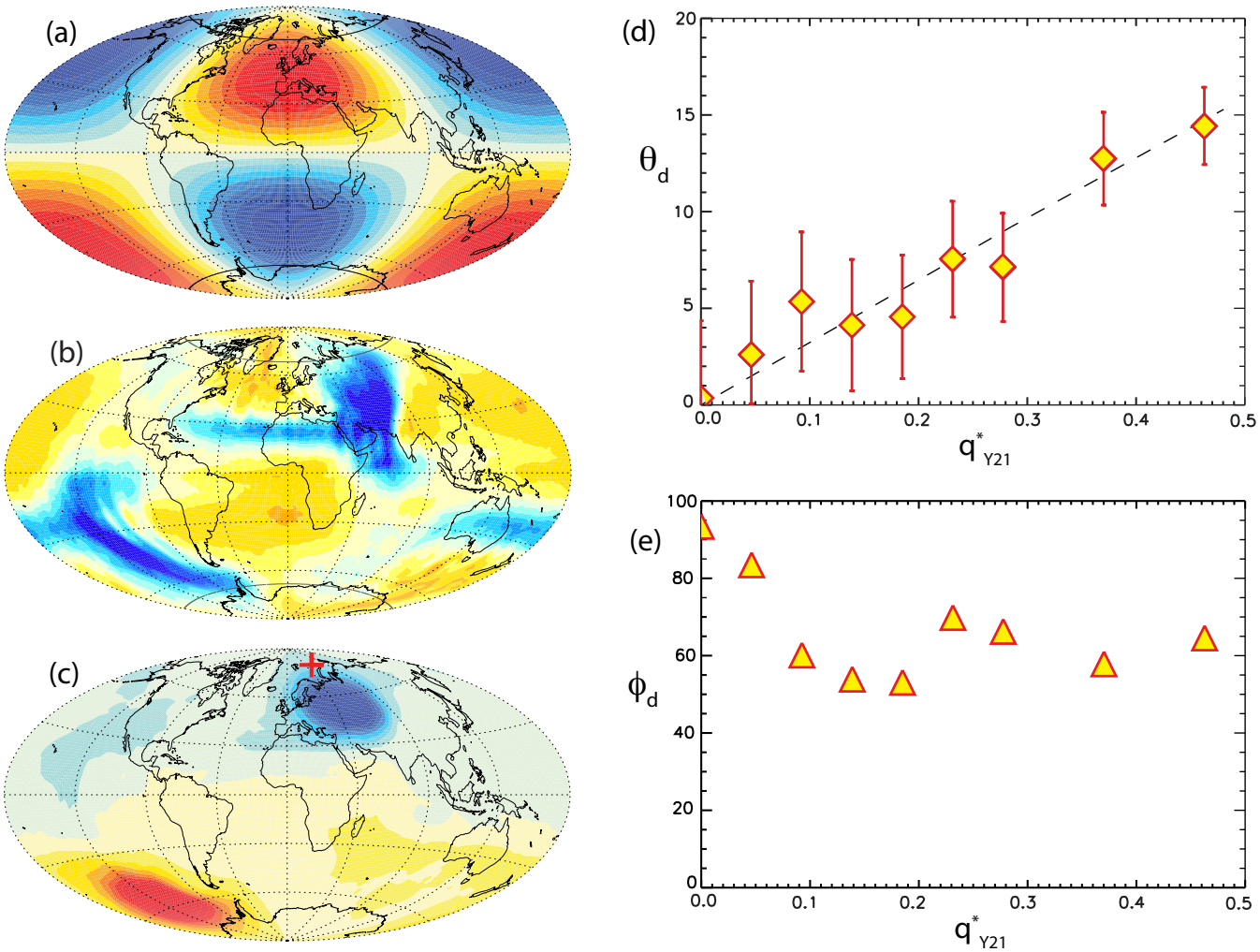

Figure 2. Sensitivity of dipole tilt to asymmetric boundary heat flux. (a) Spherical harmonic Y21 outer boundary heat flow pattern with dimensionless amplitude q^*_{21}=0.37. (b) Time average radial velocity at radius $r = 0.95$. Contour interval is 1.1 Reynolds number units. (c) Time average radial magnetic field on the outer dynamo boundary driven by the heat flux in (a); red cross marks the dipole axis location of the time average field. Contour interval is 0.25 Elsasser number units. (d) Dipole axis tilt angle θ_d versus dimensionless amplitude of the Y21 outer boundary heat flux. Dashed line shows best-fitting linear proportionality $\theta_d = 30q^*_{21}$. (e) Dipole axis longitude ϕ_d measured relative to the boundary heat flux maximum versus boundary heat flux amplitude.

The clockwise Mesozoic rotation just described is somewhat larger in magnitude but opposite in direction to the implied dipole rotations in Figs 4(a) and (b), and its timing is earlier by 30–40 million years. However, the uncertainty in the timing of the dipole rotation in Fig. 4 is several tens of million years, given the large number of assumptions built into the mantle GCM. We suggest, therefore, that global rotations in the Mesozoic, previously interpreted as polar wander, may have included rotations of the geomagnetic dipole in the opposite direction.

On theoretical grounds, it is likely that polar wander and dipole wander are dynamically coupled because both phenomena are sensitive to Y21 mantle heterogeneity. True polar wander is sensitive to the Y21 component of mantle density heterogeneity through its geoid anomaly (Ricard *et al.* 1993; Tsai & Stevenson 2007), whereas Figs 2 and 4(c) demonstrate that true dipole wander is sensitive to CMB heat flux in that same component. Because of this coupling, the true dipole wander in our dynamos is likely affected by the axial dipole assumption used in reconstructing the plate motions in the mantle GCM. The plate reconstruction by Seton *et al.* (2012) that produced the 0–200 Ma surface velocity boundary conditions used for Figs 3 and 4 adopts a mantle reference frame that includes Mesozoic rotations of the continents. The CMB heat flux pattern in a mantle GCM without these rotations might be different, which in turn would affect our dynamo-calculated dipole tilt.

To quantify the errors involved in this coupling, we rotated the CMB heat flux patterns prior to 150 Ma by 18° in the clockwise direction around an equatorial axis located at 15°W Longitude. This clockwise rotation with age is equivalent to a counterclockwise rotation of the mantle in time. It is intended to remove the major Mesozoic rotation of the continents included in Seton *et al.* (2012) and in our mantle GCM. By doing so, we obtain a model for the CMB heat flux if no true polar wander occurred. We find that the amplitude of the Y21 CMB heat flux is increased by approximately 30 per cent by this rotation. Assuming that dipole tilt is linearly related to the amplitude of the Y21 boundary heat flux component as in Fig. 2(d), we expect an increase of 2°–5° in dipole tilt from this correction. This yields a dipole tilt in the range 9°–25° during the period 150–225 Ma. Therefore, using a mantle GCM with no

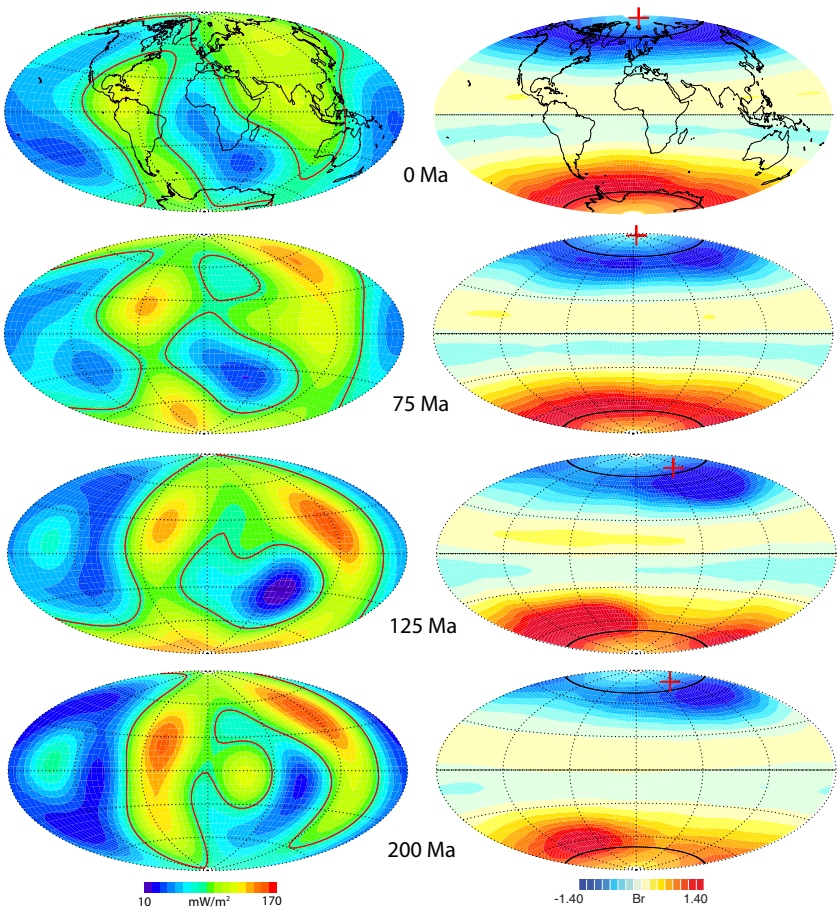

Figure 3. (a) Core–mantle boundary (CMB) heat flux from the mantle global circulation model (GCM) described in the text, at four epochs. CMB heat flux patterns are truncated at spherical harmonic degree and order $\ell = m = 4$. (b) Time average normal polarity radial magnetic field on CMB from numerical dynamos driven by the corresponding CMB heat flux patterns. Red crosses indicate the locations of the geomagnetic pole (dipole axis) of the time average normal polarity field. Radial magnetic field intensity contour interval is 0.3 Elsasser number units.

continent rotation would increase the amount of true dipole wander in our dynamos.

On even longer timescales, Torsvik *et al.* (2012) find that counterclockwise and clockwise rotations of the continents nearly balance, such that their cumulative rotation since early Carboniferous is essentially zero. One explanation for this behaviour is that true polar wander events are limited by the stabilizing effects of lower mantle density heterogeneity, which, it is assumed, has remained unchanged for hundreds of millions of years (Dziewonski *et al.* 2010). Our results suggest a simpler explanation. Because dipole tilt is dynamically constrained by the effects of Coriolis accelerations on core flows (Jones 2015), the dipole axis tends to align with Earth's spin axis. As the large-scale heterogeneity of the convecting mantle evolves (Zhong *et al.* 2007), the time average dipole axis rotates away from Earth's spin axis when the CMB heat flux is asymmetric, but then rotates back towards the spin axis when the CMB heat flux becomes more symmetric. This naturally limits the amplitude of true dipole wander. In particular, CMB heat flux heterogeneity would have to be significantly larger than mantle GCM predictions in order to support dipole tilts of 45° or more, so that extremely large apparent polar motions (∼90° in latitude, e.g.) are unlikely to be due to dipole rotation alone.

Dipole wander can be tested against polar wander using reconstructions of palaeogeography and palaeoclimate that assume a geocentric axial dipole field *a priori*, as well as stratigraphically. Fig. 1 illustrates the basic principle. With true polar wander and an axial dipole, palaeomagnetic directions correctly locate the climate equator, and climate zones appear to move north or south relative to the continents over time. With true dipole wander but no polar wander, the same palaeomagnetic directions incorrectly locate the climate equator, and the climate zones appear to move with the continents over time. Put another way, dipole wander produces systematic errors in the reconstructed climate. These errors appear as an inclination of the inferred climate equator relative to the geographic equator, a spherical harmonic Y21 pattern of climate heterogeneity, and climate zones fixed to continents moving relative to the equator, all artefacts of the axial dipole assumption.

Reconstructions based on palaeomagnetic directions usually locate the mean climate equator close to the geographic equator (Kent & Olsen 2000), but because of local and regional irregularities and limited geographical coverage, it would be a challenge to measure the inclination of the palaeoclimate equator, and still more of a challenge to resolve its palaeoclimate spherical harmonic content. That said, global palaeoclimate reconstructions often show $m = 1$ azimuthal heterogeneity prior to and after Pangea breakup, which largely disappear at later times (Ziegler *et al.* 2003). This $m = 1$ climate heterogeneity is usually attributed to a global monsoon during Pangea that weakens because of continent breakup and opening of the Atlantic Ocean, although we note that the $m = 1$ heterogeneity disappears from these climate reconstructions much later, typically

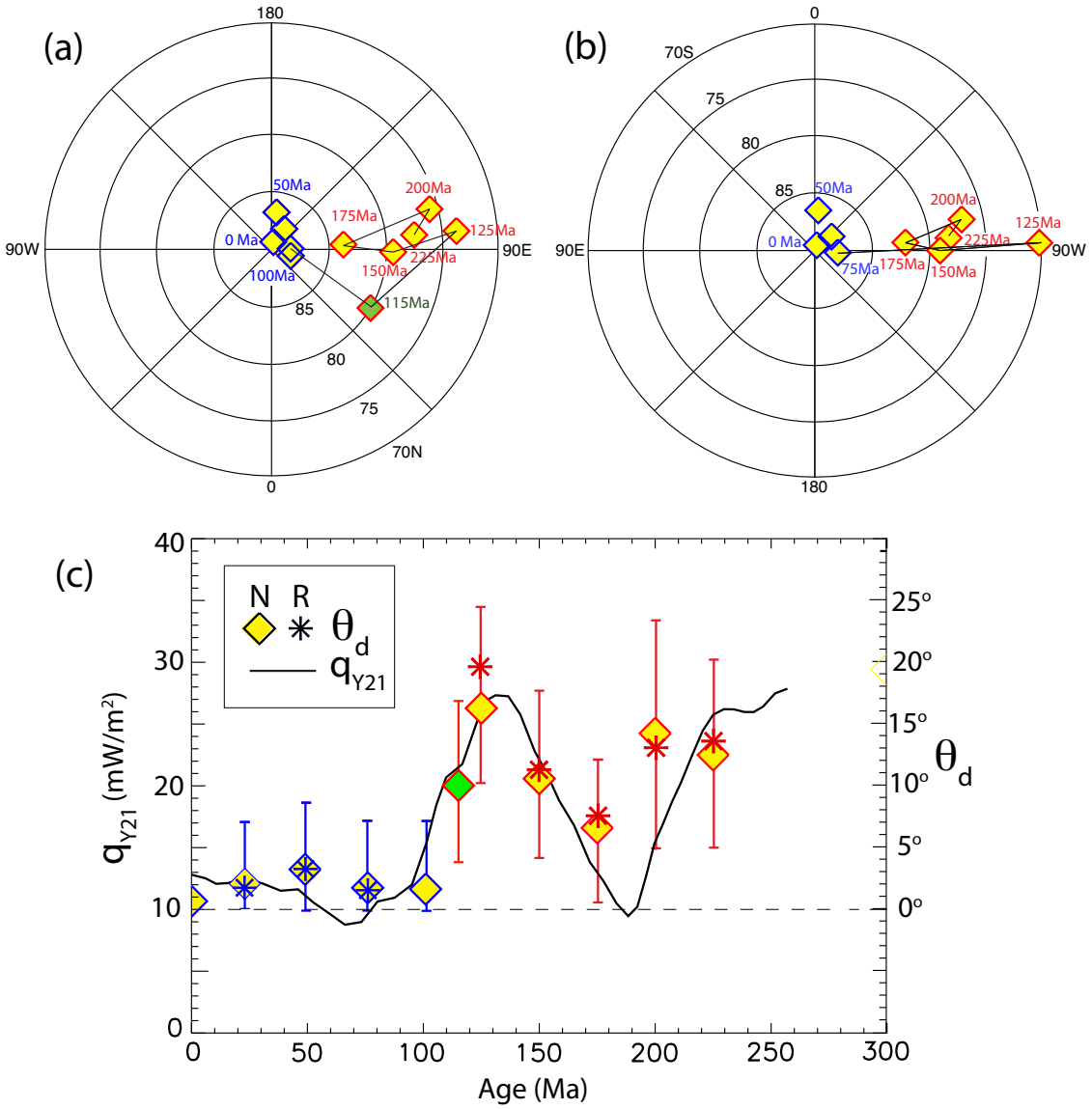

Figure 4. (a) Dipole axis locations of the time average normal polarity magnetic field at various epochs, from dynamos driven by the mantle GCM described in the text. Colour coding indicates groups of similar dipole axis locations, red = prior to, blue = after, green = during the major anticlockwise dipole rotation, respectively. North polar projection. (b) Same as (a) but for reverse polarity dipole axis locations. (c) Y21 CMB heat flux heterogeneity (peak-to-peak amplitude) from the mantle GCM described in the text (solid line) compared with dynamo-calculated time average reverse and normal polarity dipole axis tilt angle (symbols) at various epochs. Error bars are standard deviations of dipole tilt at each epoch. Symbol colours are the same as in (a).

around 120 Ma, about the time our dynamo models predict the geomagnetic dipole rotated back to its axial position.

A more specific test is the correlation between stratigraphic and palaeoinclination variations at individual sites. For example, Muttoni & Kent (2016) argue that true polar wander explains stratigraphy related to Persian Gulf oil formation on the basis of apparent climate zone shifts recorded in sediments but caused by the southward motion of Arabia away from the equator between 160 and 145 Ma. In contrast, stratigraphic sequences at sites that have large palaeoinclination variations but lack corresponding evidence of apparent climate zone shifts would be more consistent with a fixed palaeolatitude overprinted by true dipole wander.

ACKNOWLEDGEMENTS

This research was supported by Frontiers in Earth System Dynamics grant no. EAR-1135382 from the National Science Foundation and the European Union Horizon 2020 Research and Innovation Program under the Marie Sklodowska-Curie grant no. 703767. The dynamo calculations were made at the Maryland Advanced Research Computer Center (MARCC). We thank Dennis Kent and an anonymous referee for constructive reviews and Andrew Biggin for pointing out similarities between dipolar and polar wanderings.

Author contributions: PO and ML designed the numerical experiments, ER did the computations and produced the data products, PO and ML analysed the data and wrote the paper.

REFERENCES

Besse, J. & Courtillot, V., 2002. Apparent and true polar wander and the geometry of the geomagnetic field over the last 200 Myr, *J. geophys. Res.,* **107,** EPM 6–1-EPM 6-31.

Bloxham, J., 2000. Sensitivity of the geomagnetic axial dipole to thermal core–mantle interactions, *Nature,* **405,** 63–65.

Christensen, U., Aubert, J. & Hulot, G., 2010. How to make an Earth-like dynamo, *Earth planet. Sci. Lett.,* **296,** 487–496.

Dziewonski, A.M., Lekic, V. & Romanowicz, B.A., 2010. Mantle anchor structure: an argument for bottom up tectonics, *Earth planet. Sci. Lett.,* **299,** 69–79.

Evans, D.A., 2003. True polar wander and supercontinents, *Tectonophysics,* **362,** 303–320.

Fu, R.R. & Kent, D.V., 2018. Anomalous Late Jurassic motion of the Pacific Plate with implications for true polar wander, *Earth planet. Sci. Lett.,* **490,** 20–30.

Gillet, N., Jault, D., Finlay, C.C. & Olsen, N., 2013. Stochastic modelling of the Earth's magnetic field: inversion for covariances over the observatory era, *Geochem. Geophys. Geosyst.,* **14,** 766–786 .

Heimpel, M. & Evans, M., 2013. Testing the geomagnetic dipole and reversing dynamo models over Earth's cooling history, *Phys. Earth planet. Inter.,* **224,** 124–131.

Johnson, C.L. & Constable, C.G., 1997. The time-averaged geomagnetic field: global and regional biases for 0-5 Ma, *Geophys. J. Int.,* **131,** 643–666.

Johnson, C.L. & McFadden, P., 2015. The time-averaged field and paleosecular variation, in *Treatise on Geophysics,* pp. 385–417, ed. Schubert, G., Elsevier.

Johnson, C.L. *et al.*, 2008. Recent investigations of the 0–5 Ma geomagnetic field recorded by lava flows, *Geochem. Geophys. Geosyst.,* **9**(4).

Jones, C.A., 2015. Thermal and compositional convection in the core, in *Treatise on Geophysics,* pp. 115–159, ed. Schubert, G., Elsevier.

Jurdy, D.M. & Van Der Voo, R., 1975. True polar wander since the early Cretaceous, *Science,* **187,** 1193–1196.

Kelly, P. & Gubbins, D., 1997. The geomagnetic field over the past 5 Myr, *Geophys. J. Int.,* **128,** 315–330.

Kent, D.V. & Olsen, P.E., 2000. Magnetic polarity stratigraphy and paleolatitude of the Triassic-Jurassic Blomidon Formation in the Fundy basin (Canada): implications for early Mesozoic tropical climate gradients, *Earth planet. Sci. Lett.,* **179,** 311–324.

Kent, D.V., Kjarsgaard, B.A., Gee, J.S., Muttoni, G. & Heaman, L.M., 2015. Tracking the Late Jurassic apparent (or true) polar shift in U-Pb-dated kimberlites from cratonic North America (Superior Province of Canada), *Geochem. Geophys. Geosyst.,* **16,** 983–994.

Korte, M. & Holme, R., 2010. On the persistence of geomagnetic flux lobes in global Holocene field models, *Phys. Earth planet. Inter.,* **182,** 179–186.

Labrosse, S., 2003. Thermal and magnetic evolution of the Earth's core, *Phys. Earth planet. Inter.,* **140,** 127–143.

Landeau, M., Aubert, J. & Olson, P., 2017. The signature of inner-core nucleation on the geodynamo, *Earth planet. Sci. Lett.,* **465,** 193–204.

McElhinny, M.W., McFadden, P.L. & Merrill, R.T., 1996. The time averaged paleomagnetic field 0–5 Ma, *J. geophys. Res.,* **101,** 25 007–25 027.

Muttoni, G. & Kent, D.V., 2016. A novel plate tectonic scenario for the genesis and sealing of some major Mesozoic oil fields, *GSA Today,* **26**(12), 4–10.

Nilsson, A., Muscheller, R. & Snowball, I., 2011. Millennial scale cyclicity in the geodynamo inferred from a dipole tilt reconstruction, *Earth planet. Sci. Lett.* **311,** 299–305.

Olson, P. & Deguen, R., 2012. Lopsided inner core growth and eccentricity of the geomagnetic dipole, *Nat. Geosci.,* **5**(8), 565–569.

Olson, P., Deguen, R., Hinnov, L.A. & Zhong, S., 2013. Controls on geomagnetic reversals and core evolution by mantle convection in the Phanerozoic, *Phys. Earth planet. Inter.,* **214,** 87–103.

Olson, P., Landeau, M. & Reynolds, E., 2017. Dynamo tests for stratification below the core-mantle boundary, *Phys. Earth planet. Inter.,* **271,** 1–18.

Ricard, Y., Spada, G. & Sabadini, R., 1993. Polar wandering of a dynamic Earth, *Geophys. J. Int.,* **113,** 284–298.

Rudolph, M. & Zhong, S.J., 2014. History and dynamics of net rotation of the mantle and lithosphere, *Geochem. Geophys. Geosyst.,* **15,** 3645–3657

Schneider, D.A. & Kent, D.V., 1990. The time-averaged paleomagnetic field, *Rev. Geophys.,* **28,** 71–96.

Seton, M. *et al.*, 2012. Global continental and ocean basin reconstructions since 200 Ma, *Earth-Sci. Rev.,* **113,** 212–270.

Steinberger, B. & Torsvik, T.H., 2008. Absolute plate motions and true polar wander in the absence of hotspot tracks, *Nature,* **452,** 620–623.

Torsvik, T.H. *et al.*, 2012. Phanerozoic polar wander, palaeogeography and dynamics, *Earth-Sci. Rev.,* **114,** 325–368.

Tsai, V.C. & Stevenson, D.J., 2007. Theoretical constraints on true polar wander, *J. geophys. Res.,* **112,** doi:10.1029/2005JB003923.

Veikkolainen, T. & Pesonen, L., 2014. Palaeosecular variation, field reversals and the stability of the geodynamo in the Precambrian, *Geophys. J. Int.,* **199,** 1515–1526.

Wicht, J., 2002. Inner-core conductivity in numerical dynamo simulations, *Phys. Earth planet. Inter.,* **132,** 281–302.

Zhong, S.J. & Rudolph, M.L., 2015. On the temporal evolution of long-wavelength mantle structure of the Earth mantle since the early Paleozoic, *Geochem. Geophys. Geosyst.,* **16,** 1599–1615.

Zhong, S.J., Zhang, N., Li, Z.-X. & Roberts, J.H., 2007. Supercontinent cycles, true polar wander, and very long-wavelength mantle convection, *Earth planet. Sci. Lett.,* **261,** 551–564.

Ziegler, A.M., Eshel, G., Rees, P.M., Rothfus, T., Rowley, D. & Sunderlin, D., 2003. Tracing the tropics across land and sea: permian to present, *Lethaia,* **36,** 227–254.

SUPPORTING INFORMATION

Supplementary data are available at *GJI* online.

Figure S1. Geomagnetic pole locations at epochs 225 Ma (a) and 0 Ma (b) from dynamos driven by the mantle GCM described in the text. Yellow squares are the geomagnetic poles of the time average normal polarity magnetic fields. Green squares are the time average geomagnetic poles, the average locations of the instantaneous poles marked by green dots. North polar projections, normal polarity data only.

Please note: Oxford University Press is not responsible for the content or functionality of any supporting materials supplied by the authors. Any queries (other than missing material) should be directed to the corresponding author for the article.

Key words

Authors are requested to choose key words from the list below to describe their work. The key words will be printed underneath the summary and are useful for readers and researchers. Key words should be separated by a semi-colon and listed in the order that they appear in this list. An article should contain no more than six key words.

COMPOSITION and PHYSICAL PROPERTIES
Composition and structure of the continental crust
Composition and structure of the core
Composition and structure of the mantle
Composition and structure of the oceanic crust
Composition of the planets
Creep and deformation
Defects
Elasticity and anelasticity
Electrical properties
Equations of state
Fault zone rheology
Fracture and flow
Friction
High-pressure behaviour
Magnetic properties
Microstructure
Permeability and porosity
Phase transitions
Plasticity, diffusion, and creep

GENERAL SUBJECTS
Core
Gas and hydrate systems
Geomechanics
Geomorphology
Glaciology
Heat flow
Hydrogeophysics
Hydrology
Hydrothermal systems
Infrasound
Instrumental noise
Ionosphere/atmosphere interactions
Ionosphere/magnetosphere interactions
Mantle processes
Ocean drilling
Structure of the Earth
Thermochronology
Tsunamis
Ultra-high pressure metamorphism
Ultra-high temperature metamorphism

GEODESY and GRAVITY
Acoustic-gravity waves
Earth rotation variations
Geodetic instrumentation
Geopotential theory
Global change from geodesy
Gravity anomalies and Earth structure
Loading of the Earth
Lunar and planetary geodesy and gravity
Plate motions
Radar interferometry
Reference systems
Satellite geodesy
Satellite gravity
Sea level change
Seismic cycle
Space geodetic surveys
Tides and planetary waves
Time variable gravity
Transient deformation

GEOGRAPHIC LOCATION
Africa
Antarctica
Arctic region
Asia
Atlantic Ocean
Australia
Europe
Indian Ocean
Japan
New Zealand
North America
Pacific Ocean
South America

GEOMAGNETISM and ELECTROMAGNETISM
Archaeomagnetism
Biogenic magnetic minerals
Controlled source electromagnetics (CSEM)
Dynamo: theories and simulations
Electrical anisotropy
Electrical resistivity tomography (ERT)
Electromagnetic theory
Environmental magnetism
Geomagnetic excursions
Geomagnetic induction
Ground penetrating radar
Magnetic anomalies: modelling and interpretation
Magnetic fabrics and anisotropy
Magnetic field variations through time
Magnetic mineralogy and petrology
Magnetostratigraphy
Magnetotellurics
Marine electromagnetics
Marine magnetics and palaeomagnetics
Non-linear electromagnetics
Palaeointensity
Palaeomagnetic secular variation
Palaeomagnetism
Rapid time variations
Remagnetization
Reversals: process, time scale, magnetostratigraphy
Rock and mineral magnetism
Satellite magnetics

GEOPHYSICAL METHODS
Downhole methods
Fourier analysis
Fractals and multifractals
Image processing
Instability analysis
Interferometry
Inverse theory
Joint inversion
Neural networks, fuzzy logic
Non-linear differential equations
Numerical approximations and analysis
Numerical modelling
Numerical solutions
Persistence, memory, correlations, clustering
Probabilistic forecasting
Probability distributions
Self-organization
Spatial analysis
Statistical methods
Thermobarometry
Time-series analysis
Tomography
Waveform inversion
Wavelet transform

PLANETS
Planetary interiors
Planetary volcanism

SEISMOLOGY
Acoustic properties
Body waves
Coda waves
Computational seismology
Controlled source seismology
Crustal imaging
Earthquake dynamics
Earthquake early warning
Earthquake ground motions
Earthquake hazards
Earthquake interaction, forecasting, and prediction
Earthquake monitoring and test-ban treaty verification
Earthquake source observations
Guided waves
Induced seismicity
Interface waves
Palaeoseismology
Rheology and friction of fault zones
Rotational seismology
Seismic anisotropy
Seismic attenuation
Seismic instruments
Seismic interferometry
Seismicity and tectonics
Seismic noise
Seismic tomography
Site effects
Statistical seismology
Surface waves and free oscillations
Theoretical seismology

Tsunami warning
Volcano seismology
Wave propagation
Wave scattering and diffraction

TECTONOPHYSICS
Backarc basin processes
Continental margins: convergent
Continental margins: divergent
Continental margins: transform
Continental neotectonics
Continental tectonics: compressional
Continental tectonics: extensional
Continental tectonics: strike-slip and transform
Cratons
Crustal structure
Diapirism
Dynamics: convection currents, and mantle plumes
Dynamics: gravity and tectonics
Dynamics: seismotectonics
Dynamics and mechanics of faulting
Dynamics of lithosphere and mantle
Folds and folding
Fractures, faults, and high strain deformation zones
Heat generation and transport
Hotspots
Impact phenomena
Intra-plate processes
Kinematics of crustal and mantle deformation
Large igneous provinces
Lithospheric flexure
Mechanics, theory, and modelling
Microstructures
Mid-ocean ridge processes
Neotectonics
Obduction tectonics
Oceanic hotspots and intraplate volcanism
Oceanic plateaus and microcontinents
Oceanic transform and fracture zone processes
Paleoseismology
Planetary tectonics
Rheology: crust and lithosphere
Rheology: mantle
Rheology and friction of fault zones
Sedimentary basin processes
Subduction zone processes
Submarine landslides
Submarine tectonics and volcanism
Tectonics and climatic interactions
Tectonics and landscape evolution
Transform faults
Volcanic arc processes

VOLCANOLOGY
Atmospheric effects (volcano)
Calderas
Effusive volcanism
Eruption mechanisms and flow emplacement
Experimental volcanism
Explosive volcanism
Lava rheology and morphology
Magma chamber processes
Magma genesis and partial melting
Magma migration and fragmentation
Mud volcanism
Physics and chemistry of magma bodies
Physics of magma and magma bodies
Planetary volcanism
Pluton emplacement
Remote sensing of volcanoes
Subaqueous volcanism
Tephrochronology
Volcanic gases
Volcanic hazards and risks
Volcaniclastic deposits
Volcano/climate interactions
Volcano monitoring
Volcano seismology